Editors' Suggestion

Vacuum chambers for Swiss Light Source arcs

R. Ganter, P. Braschoss, H.-H. Braun, J. Buchmann, A. Citterio, M. Dehler, N. Gaiffi, N. Kirchgeorg, M. Magjar, C. Rosenberg, D. Stephan, L. Schulz, R. Sieber, X. Wang, and A. Zandonella

Paul Scherrer Institute, Villigen, Switzerland

(Received 21 February 2024; accepted 19 April 2024; published 10 May 2024)

The vacuum chambers for diffraction limited storage ring differ from the previous storage rings generation in three main aspects: the cross-section dimension, which is divided by a factor of 2 or more to fit smaller magnet apertures; the material, which includes much more copper for heat dissipation and to limit resistive wakefields; the coating of the inner surface with a nonevaporable getter (NEG) to ensure good pumping level despite low conductance. This paper gives a detailed description of the vacuum chambers' design used in the arc section of SLS 2.0, starting with conceptual design choices based among others on synchrotron radiation heat and wakefield considerations. The particular case of the main bending magnet vacuum chamber is explained in detail from design to manufacturing, including the development of an appropriate NEG coating procedure. Finally, the overall assembly of a 17 m long arc, its activation to reach pressure in the 10^{-11} mbar range followed by transport and installation into the magnets is presented. This validates the choice of *ex situ* activation for an arc vessel made out of copper, with wall thicknesses as small as 1 mm and with less than 0.5 mm clearance to magnet poles.

DOI: 10.1103/PhysRevAccelBeams.27.053201

I. INTRODUCTION

In the quest for increased radiation brightness, the most recent synchrotron facilities [1–3] are based on magnet lattices with much more dipole magnets per unit cell than in the previous generation of the storage ring. Many existing facilities are preparing upgrade programs with multibend lattices [4–13]. The SLS 2.0 synchrotron storage ring currently under construction at PSI aims to increase the radiation brightness by a factor of at least 40 in comparison to the previous SLS storage ring [14]. Such an increase will be achieved by reducing the horizontal emittance and improving the undulator performances [15]. Brightness is inversely proportional to the horizontal electron beam emittance, which is proportional to the third power of dipole bending angles per unit cell of a lattice [16–18]. Therefore, the so-called diffraction limited storage rings have many more bending magnets with smaller angles per arc. SLS 2.0 will have seven longitudinal gradient bending magnets [19] together with 14 reverse bend magnets per arc [20]. The overall storage ring circumference and arc lengths stay unchanged such that the density of magnets per arc increases significantly in comparison to the previous SLS storage ring. To reach the required deflection in short length magnets, it is necessary to decrease the magnetic aperture diameter. This aperture reduction turns into small cross-section vacuum chambers with bad pumping conductance, requiring nonevaporable getter (NEG) coating [21,22]. Not only does the pumping conductance become an issue with a smaller vacuum chamber cross section, but also the heat dissipated by the synchrotron radiation on the vacuum vessel is more problematic. In addition, the inner cross-section geometry is more sensitive to beam wakefield issues like broadband impedances or higher order modes trapping. In this paper, the first part describes the general vacuum concept of the SLS 2.0 arcs. In the second part, the detailed design of the bending magnet vacuum chambers is explained. Finally, the overall arc assembly and vacuum performance are presented in the last section.

II. OVERALL VACUUM CONCEPT

The SLS 2.0 storage ring circumference is identical to the previous SLS ring at 288 m distributed in 12 identical 17 m long arcs and 12 straight sections of various lengths (Fig. 1). Four arcs (ARS01; ARS02, ARS06, and ARS10) will be equipped with so-called "superbend" magnets at the location of the central bending dipole (dipole A). For day 1, these superbend magnets will consist of permanent magnet-based dipoles (Bmax = 2T) with a smaller gap requiring a vacuum chamber with a smaller inner height than all other dipole chambers. In the second phase of the SLS2.0 project, two superbend permanent magnets (ARS01 and ARS02)

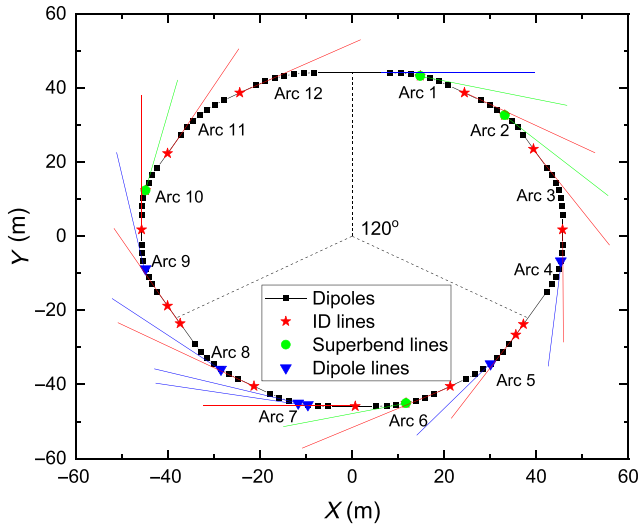

FIG. 1. Layout of the SLS2.0 storage ring, only arcs 1 and 2 will be equipped with superconducting dipole magnets.

will be exchanged with superconducting dipole magnets with a warm vacuum chamber going through a cryostat. This implies venting these two arcs *in situ*, when the chamber string is already installed in the magnets without the possibility of baking afterward since there is no bellow to compensate for dilatation in an arc. The straight sections have three different lengths denominated as: (i) short straights: 2S, 4S, 6S, 8S, 10S, and 12S (4.31 m long); (ii) middle straights: 3M, 7M and 11M (6.55 m long); (iii) long straights: 1L, 5L, and 9L (12.71 m long).

While the circumference of the storage ring vacuum chamber stays the same, the cross section becomes much smaller in SLS 2.0 as depicted in Fig 2. This is the direct consequence of the smaller magnet apertures required to pack all magnets of the seven-bend achromat lattice.

A. Design choices

The design of the SLS2.0 vacuum chambers is based on the following choices: (i) The electron channel cross section has an octagonal shape with 18 mm between

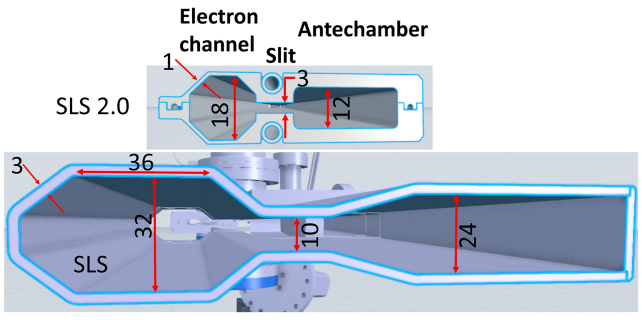

FIG. 2. Typical cross sections of the bending magnet vacuum chambers in the arc for SLS 2.0 (top) and SLS (bottom). Most important dimensions are indicated in millimeters.

opposite faces, and a slit opening of only 3 mm height allows the synchrotron radiation fan to reach the antechamber (see Fig. 2). This slit is, however, larger (10 mm height), in the first dipole chamber of each arc, to allow better extraction of the light coming from the undulators. The octagonal shape facilitates the integration of beam position monitors (BPM) where the flat pickup heads are located in the 45° planes. The wall is a minimum of 1 mm thick, typically with a distance of 1 mm from the magnet poles, but at several locations, this distance goes down to 0.2 mm. Due to tolerances, there are contacts at various places between the vacuum chamber and the magnet poles. (ii) The main reason for choosing copper as the material of the vacuum chamber walls is its good thermal and electrical conductivity, required to minimize resistive wakefield and to dissipate heat. Apart from electrical losses, heat up is also caused by synchrotron radiation hitting the chamber surface. Copper Cu-OFE rather than Cu-OFS is used for the dipole chambers since there was already extensive experience available at PSI in brazing this type of material. All chambers are brazed in vacuum oven at a high temperature (above 860 °C), which changes the mechanical properties of copper (e.g., yield strength) leading to a relatively soft and flexible vacuum chamber (annealing). (iii) Due to the limited conductance of the 18 mm vacuum pipe cross section, a layer of nonevaporable getter (NEG) is deposited on all copper inner surfaces of the vacuum chambers. The main purpose of the NEG coating is to reduce the photon stimulated desorption (PSD) rate to speed up the vacuum conditioning time of the storage ring [21]. An inherent problem of the NEG coating is its low electrical conductivity, which may provoke single-bunch instabilities in the machine [23]. To minimize the effect, the coating thickness should be smaller than the electrical skin depths at typical frequencies within the beam spectrum. It was specified to be 500 nm ±30%. NEG alloys come in different morphologies with strongly different electrical conductivities, so the coating was validated at rf frequencies of 12 and 100 GHz [24]. The NEG composition should be 10%–50% titanium, 15%–50% zirconium, and 15%–50% vanadium to ensure an activation at 200 °C. (iv) Due to space constraints, there is no possibility to install bellows within an arc. This means that *in situ* baking is not possible. As for SLS 1, every arc is preassembled, closed with end valves, and baked in an oven before installation in the ring. The 17 m long sector (Fig. 3) is transported with a crane after baking and NEG activation and deposited on the girder while all magnets are half-open or shifted transversely (see last section). (v) Since no baking is possible *in situ*, no reactivation of the NEG layer is possible after it gets saturated in the ring. To guarantee pumping capability when the NEG layer is saturated, discrete pump systems are placed at the location of every crotch absorber: one ion getter pump (Agilent Diode Vaclon Plus 55 with 50 l/s pumping speed for N2) and a getter CapaciTorr pump

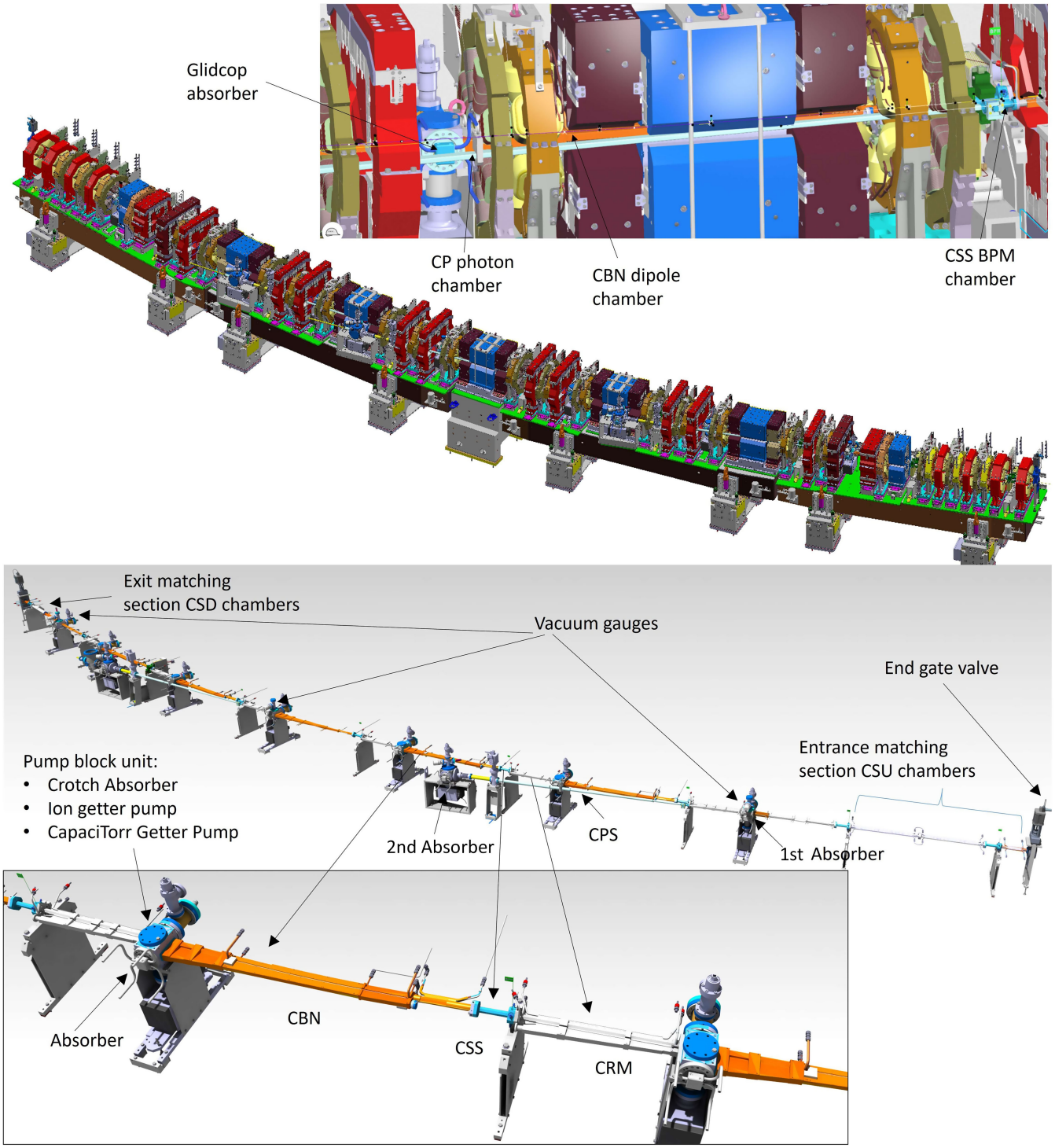

FIG. 3. 3D layout of the SLS2.0 arc showing the high density of magnets (top). Layout of the 17 m long vacuum arc string (bottom) with a closer view of the unit cell composed of three chambers CBN-CRM-CSS (see Table I).

(Z400 from SAES with about 210 l/s pumping speed for CO). In total, there are seven such pump blocks per arc (Table I). (vi) The goal of the vacuum pumping system is to reach an average pressure of 10^{-9} mbar (CO equivalent) after 100 A h of beam conditioning. This should correspond to several weeks of conditioning. While this may still cause ion stimulated beam instabilities [25], the level of these fast beam ion instabilities is sufficiently low to be suppressed with the bunch by bunch feedback system.

The large density of magnets per meter (Fig. 3) leaves little space for synchrotron radiation (SR) fan expansion, causing large SR power densities on chamber walls and

TABLE I. Main vacuum systems and quantities per arc.

Dipole chambers (CBN/CBI/CBO)	7 units/arc
BPM stainless steel chamber CSS	9 units/arc
Reverse bend chamber CRM/CRU/CRD/CRS	6 units/arc
Entrance and exit matching section (CSU/CSD)	2 units/arc
Dipole crotch absorbers	7 units/arc
Ion pumps and getter pumps in CB chambers	7 units/arc
Vacuum gauges (cold cathode IKR270)	3 units/arc
Synchrotron light extraction chambers (CPS/CPD)	2–3 units/arc
Flat gasket transitions on electron trajectory	30 units/arc

absorbers. To manage the SR heat dissipation, the following criteria have been adopted: (i) No SR on stainless steel flanges, gaskets, or BPM pickups. (ii) Less than 10 W/mm^2 on copper surfaces that are water cooled to limit at maximum any local temperature rises, which could potentially heat up permanent magnets and produce chamber dilatation that is not compensated by bellows. (iii) Less than 50 W/mm^2 or less than 400 °C on the Glidcop® crotch absorber surface [26]. (iv) Crotch absorbers are located about 0.8 m downstream of every dipole magnet center. The crotch absorbers are assembled in a stainless-steel cube, where the ion pump and the getter cartridge pump are also present. (v) With the help of a synchrotron radiation ray tracing simulation tool (SYNRAD [27]), tapering surfaces were introduced in almost every vacuum chamber in order to distribute the power density over larger surfaces. To protect the beam position monitors (BPM) in stainless steel and the flanges from overheating, the cross section is locally increased to 21 mm to stay in the shadow of upstream parts. (vi) In addition to SR heat, every small discontinuity of the vacuum vessel (e.g., seals gap) or sudden change of the inner geometry will diffract the self-field of the stored beam and cause wakefields. If trapped, the resulting resonances will cause local heat up and/or destabilize and destroy the beam via coupling oscillations.

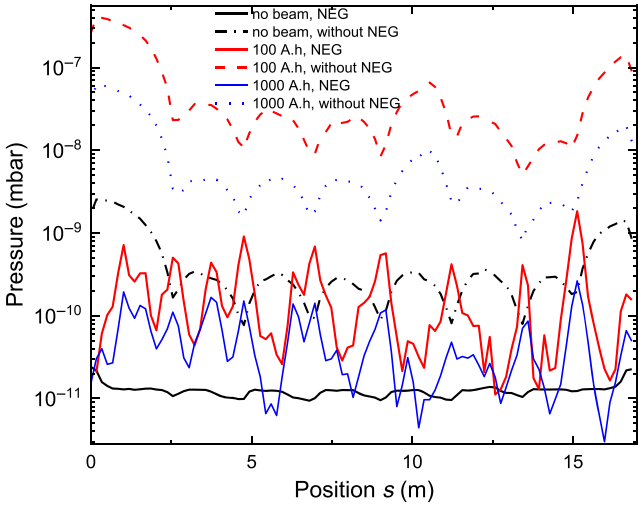

FIG. 4. Simulation of partial pressure of carbon monoxide (CO) along the electron beam orbit of an SLS2.0 arc sector (projection on the 16 m long chord defined by the arc). Cases without NEG mean without pumping effect of NEG and with the photon stimulated desorption of copper OFHC material.

The design of these transitions had to include detailed electromagnetic simulations to keep these effects under control [28].

B. Vacuum simulations

The ratio between outgassing due to photon stimulated desorption (PSD) and pumping efficiency (discrete and distributed) defines the equilibrium pressure in the SLS 2.0 storage ring during the first operation with the beam. To simulate the vacuum profile along an arc, a combination of synchrotron radiation ray tracing simulations and vacuum conductance Monte Carlo simulations using the vacuum chamber 3D design, were performed. The vacuum chambers are designed with Catia V6 (3D Experience), and 3D files are exported to the synchrotron radiation ray

TABLE II. Parameters used for the SYNRAD and MOLFLOW simulations of Fig. 4 for CO equivalent gas. The photon desorption yield (molecules per photons) provided with MOLFLOW was used for the NEG and OFHC surface simulation.

Simulation parameters	Values
Inner roughness ratio (SYNRAD)	0.004
Beam current (SYNRAD)	400 mA
Pumping speed ZAO400	210 l/s per pump or 0.95 sticking factor for 7 pumps (215 cm^2)
Pumping speed VacIon55 plus	50 l/s per pump or 0.15 sticking factor for 7 pumps (215 cm^2)
Outgassing rate (without NEG and without beam)	5×10^{-13} mbar l s^{-1} cm^{-2}
NEG sticking factor	0.005 for all NEG-coated surfaces (15 533 cm^2)
Surfaces with desorption yield of Cu OFHC	Pump blocks (7 units equivalent to 5885 cm^2) and gate valves at each arc ends (7 cm^2)
Surfaces with desorption yield of NEG	All inner surfaces except pump blocks and pumps (15 533 cm^2)
Averaged NEG photon desorption yield in facets with 1 to 10 W/cm^2 (see Fig. 5)	9×10^{-7} molecules per photon for a dose of 10^{19} photons/cm^2 (100 A h)
Averaged OFHC photon desorption yield in facets with 10^{-7} to 10^{-6} W/cm^2 (see Fig. 5)	7×10^{-5} molecules per photon for a dose of 10^{19} photons/cm^2 (100 A h)

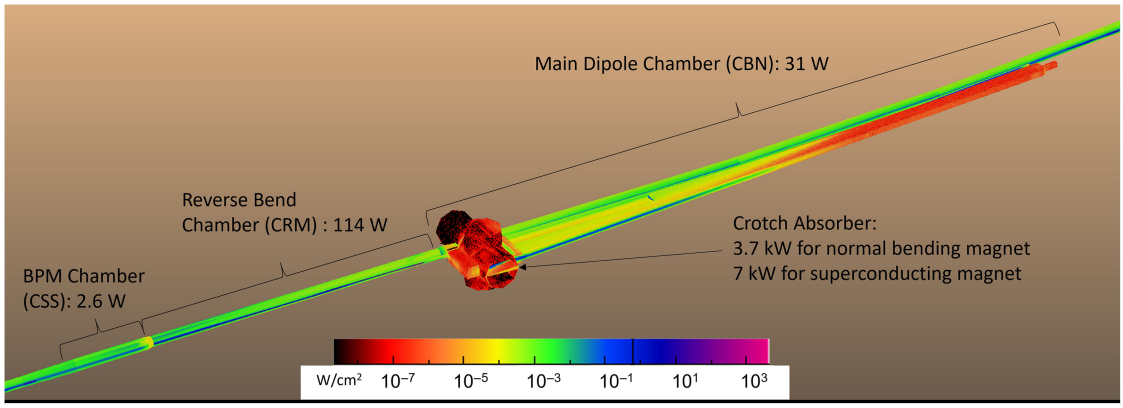

FIG. 5. Synchrotron radiation power distribution in the unit cell of an arc seen from outer ring side. The double cross chamber (red and darker) corresponds to the pump block where the crotch absorber is located.

tracing simulations tool SYNRAD V1.4.28 [27]. The different magnet regions are specified using the special Optics Builder tool provided by SYNRAD. The outgassing rate and vacuum pressure profile are finally calculated with MOLFLOW [27], importing the SR power density distribution (including reflected photons) calculated with SYNRAD.

The partial pressure profile of carbon monoxide (CO) along the electron beam trajectory in a full arc sector is presented in Fig. 4. The goal is to reach a CO partial pressure below 10^{-9} mbar to obtain a sufficiently low level of gas Bremsstrahlung in the ring and allow a safe opening of beamline shutters. The simulation has been done using the Twiss parameters of the storage ring lattice. Several cases are plotted showing the effect of the NEG coating distributed pumping for various conditioning times.

Without any beam, the pressure is about a factor of 30 smaller when NEG is presented on the surface (assuming parameters listed in Table II). The NEG layer reduces the photon stimulated desorption (PSD) and pumps molecules.

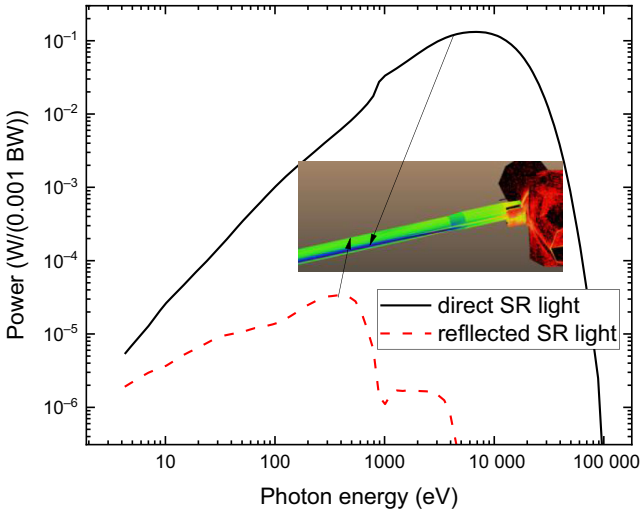

FIG. 6. Photon energy spectrum from the direct synchrotron radiation in the last chamber of an arc (CSD) and from the reflected light impinges on the top facet of the octagonal chamber.

Consequently, 100 A h is enough to be below 10^{-9} mbar equivalent CO when chambers are NEG coated as it would take a conditioning time longer than 1000 A h without NEG. This means that the benefit of NEG is faster conditioning time by at least a factor of 10.

It is interesting to notice that the seven pumping blocks appear as pressure peaks when NEG coating is presented and as valleys when no NEG pumping is included. Without NEG (or with a saturated NEG layer) only the pump blocks can reduce the pressure (valley). When the NEG layer is pumping, the pump blocks are areas with large desorption, since the crotch absorbers are sitting in the pump blocks and thus, they correspond to these maxima of pressures.

The Glidcop crotch absorbers (Fig. 5) stop 85% of the SR power generated by the bending magnets (up to 7 kW for the superbends and 3.7 kW for the normal bends). The power dissipated in the arc unit cell (2.1 m long), composed of three vacuum chambers (CSS-CBN-CTM), is about 150 W. The reflection of the synchrotron radiation is included in the simulation, considering NEG reflection properties and typical roughness of copper (equivalent to Ra $\sim$ 0.8 μm). The full chamber is illuminated with light as it can be seen in Fig. 5, but this corresponds mainly to reflected light. Direct SR light fan is mainly visible on the CRM side facet (blue strip at the bottom of Fig. 5), with about 10 W/cm^2 at maximum. The reflected photons illuminating the top or bottom surface of the chamber have less than 1000 eV (Fig. 6) of energy and the mean power is about 1 mW/cm^2. Despite the low power density level, it can also illuminate sensitive areas like the BPM buttons.

III. SEVEN BEND ACHROMATS VACUUM CHAMBERS

A. Overall arc layout

The arc sector starts and finishes with a gate valve [29]. There are 14 different types of vacuum chambers in an arc (Fig. 3), and about 500 chambers are assembled to complete the whole ring. The main bending magnet

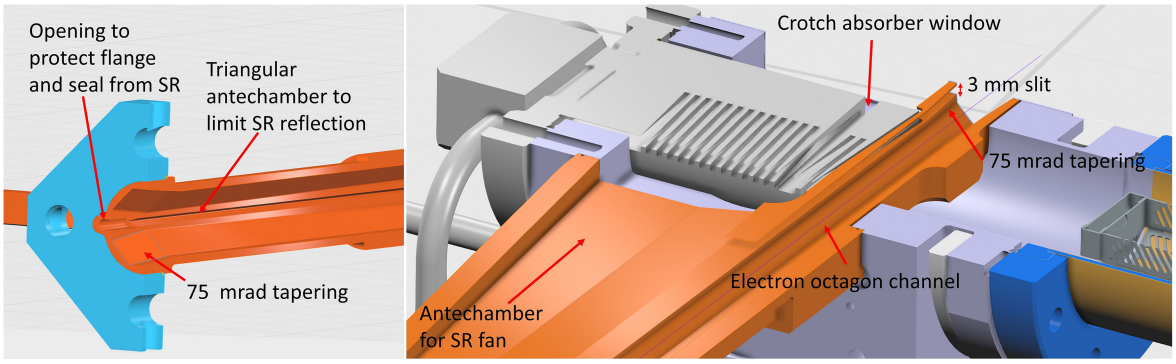

FIG. 7. Cut view of a CSD chamber at its flange extremity showing the inner geometry used to avoid direct SR on the gasket seals and to limit reflection (left drawing) and cut view of the crotch absorber installed in the CBN pump block (right drawing).

chambers (chamber bend normal, CBN) are the largest and most complex chambers of the arc. The CBN chambers include an antechamber to allow the extraction of the synchrotron radiation. To evacuate the heat, cooling channels are brazed on the chambers. The vacuum chambers are screwed together and sealed with silver-coated copper flat seals (see last section on assembly).

B. Dipole vacuum chambers

1. Design constraints

The reduction of the magnet apertures generates constraints on the vacuum chamber design: more heat dissipation due to synchrotron radiation (SR) illumination (i), an increased sensitivity to wakefields issues (ii), and finally the chamber has to be compatible with an NEG coating process (iii). Reflected synchrotron radiation is rather weak in intensity but illuminates all surfaces and can also propagate in straight sections and reach sensitive equipment, which can tolerate only little heat dissipation (e.g., superconducting undulator and fast kicker blades). To limit SR coming from arc-bending magnets into the straight sections, the side walls of the last chambers of every arc (chamber straight downstream, CSD) have a triangular shape (Fig. 7). This geometry helped to reduce the power going into the straight section downstream of an arc section from 350 to 230 W.

All transitions between different cross-section geometries have been simulated with wakefield simulation tools [28]. Indeed, the sudden changes of vacuum inner cross sections can lead to resonances between the electron bunches and the vacuum chamber. These trapped high order modes (HOM) could generate beam instabilities and/or strong local power dissipation. Figure 8 (bottom image) shows the final geometry of CBN to CRM transition, obtained to avoid both direct SR heat up of a stainless steel flange/gasket assembly (unwanted because it could lead to leaks) (i) and trapped high order modes (HOM) (ii). In an earlier version of the design, all facets of the inner octagon cross section were tapered from 18 to 21 mm, which led to trapped HOM exactly at the flange interface with more than 225 W of power dissipation (red area in Fig. 8, top). Having tapered geometry only on the side facets was the compromise to avoid strong wakefield instabilities and still protect the flange from direct SR heat up. Due to the small cross section of 18 mm, the resistive wakefield contribution of each chamber has also been included in an overall budget, considering a NEG electrical conductivity of $\sigma_{\mathrm{NEG}} = 8 \times 10^5$ S/m. As a compromise, the thickness of the NEG coating is limited to 0.5 ± 0.15 μm in the electron channel to avoid too large of a contribution to resistive wakefield SLS 2.0.

Finally, each chamber design has to be conceived to allow NEG coating of the inner surface. The bending magnet chambers have an antechamber to allow the extraction of the SR fan leading to a keyhole shape at the downstream extremity of the CBN chamber (Fig. 7). To facilitate the coating of the antechamber, a second vacuum port (DN16) is integrated on the antechamber axis so that two cathode wires (Fig. 9) can be stretched through the chamber to maximize the NEG coverage on the inner surface.

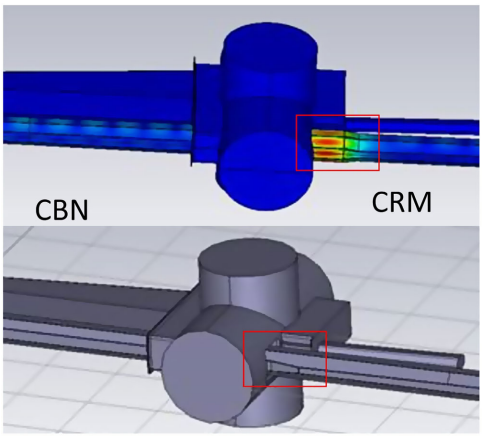

FIG. 8. 3D model of the transition from dipole chamber CBN to the downstream chamber CRM (red marked area) with tapering on all facets (top) and final design with tapering only on the horizontal plane (bottom).

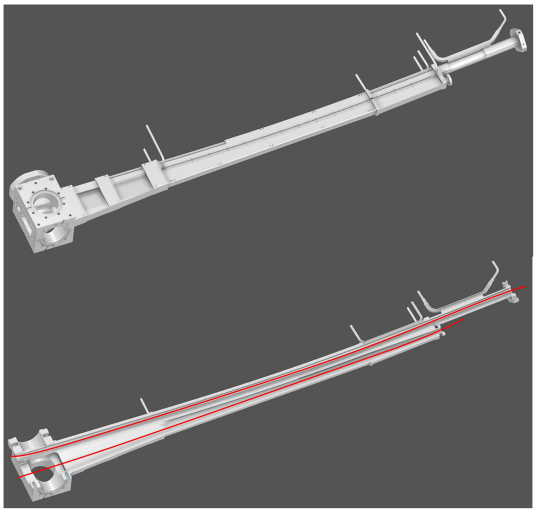

FIG. 9. 3D view of the dipole magnet chamber CBN (top) and illustration of the NEG cathode-wires (red lines) position during coating (bottom).

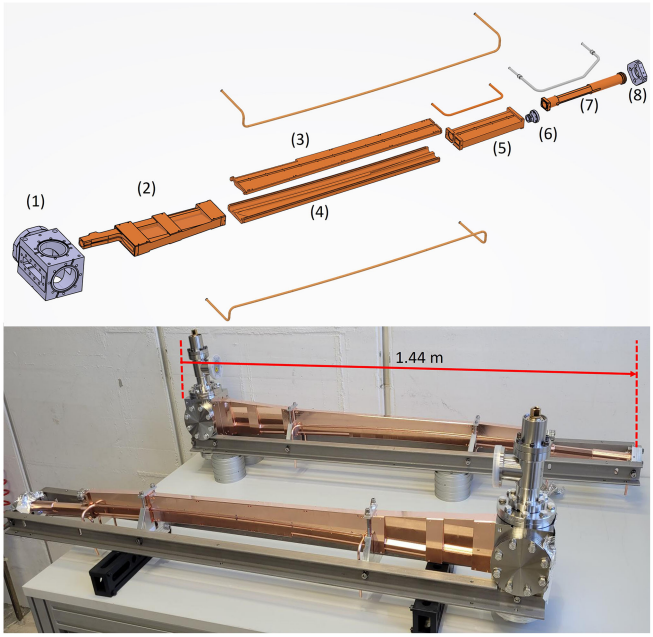

FIG. 10. Exploded view of the dipole chamber CBN (top) and pictures of two units installed in their transport stiffeners (bottom).

2. *Bending magnet chamber manufacturing procedure*

The CBN chamber starts with a simple octagonal channel of 18 mm and slowly expands with an antechamber to let the synchrotron radiation escape the electron channel in the direction of the crotch absorber. The electron channel is curved in the central part of the chamber to follow the electron beam orbit within the main bending magnet. This central part of the chamber (600 mm long) is made from two halves of copper plates precisely milled to the required geometry and thickness [parts (3) and (4) in Fig. 10]. A roughness better than Ra $\sim$ 0.8 μm is achieved by milling (Table III). The precision of the inner geometry has been achieved by using several sequences of annealing and milling. Negative shapes of the outer surface, which matches the half shell exactly, were produced to uniformly hold the part by aspiration during the milling work. The upstream and downstream parts of the CBN chamber [parts (2), (5), and (7) in Fig. 10] are produced thanks to a combination of milling and wire erosion of the inner cross section. Finally, all these copper parts are brazed together with stainless steel flanges and a DN63 cube [parts (1), (6), and (8) in Fig. 10]. High purity (99.99%) copper Cu-OFE (UNS C10100) forged in all three directions is used as raw material, and 3D-forged stainless steel 316 LN (1.4429) is used for the end flanges and the pump cube.

The brazing procedure is done in two steps (Fig. 11), where the last step requires a large vacuum oven to install the chamber vertically (1.44 m long). During the process, the parts are maintained together by gravity under their own weight, and no pressing loads are used to avoid unwanted deformation during the dilatation process as it was observed in a first prototype test. During brazing, the temperature of the copper reaches 850 °C, which causes the copper to become very soft. The chamber is then particularly fragile, with a heavy stainless-steel block on one end and areas with only one mm thick copper walls in the middle of the chamber. A transport steel stiffener is installed around the chamber (Fig. 10) shortly after brazing to avoid accidental deformation during manipulation.

TABLE III. Main parameters of the arc vacuum chambers.

Main parameters		Comments
Copper material	Cu-OFE (UNS C10100)	Yield strength ~25 MPa at room temperature after brazing cycle
Inner roughness	Ra = 0.8 μm	
Minimum wall thickness	1 mm	
Minimum distance to magnet poles	1 mm	0.2 mm to poles at some locations
Minimum distance to magnet coil	5 mm	2.5 mm to coil at some location
NEG thickness	0.5 μm ± 30%	
Stainless steel	316LN and 3D forged	
Cooling channel inner diameter	4 mm	
Water flow maximum speed	1.5 m/s	

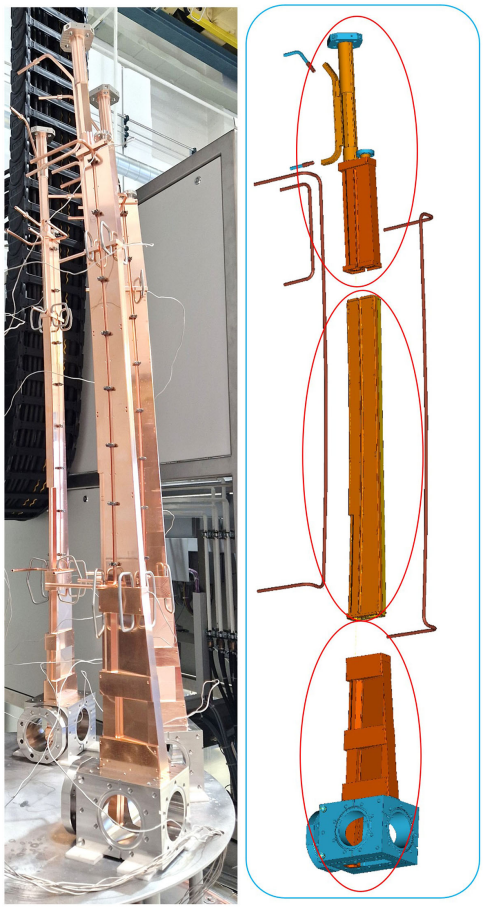

FIG. 11. Dipole chamber installed vertically in the brazing oven (left) the brazing procedure is done in two steps: red marked in the first step and blue marked in the second step (right).

After production of the first few CBN chambers, we found out that the chambers experience local plastic deformation, up to 0.5 mm, during the first pump down and in areas with the largest width (chamber portion 2 in Fig. 10). In addition, every bakeout cycle was increasing this local plastic deformation by another 0.1 mm. This was unfortunately not expected and not anticipated by our finite element analysis due to insufficient fine meshing. To avoid this plastic deformation, an additional step was then developed, tested, and added to the production procedure: after first pump down, the chamber is slowly filled with about 2.5 bar of nitrogen to recover the original dimensions. This nitrogen overpressure acts like a mechanical cold working of copper walls such that no significant plastic deformation is observed in the next pump down. The elastic deformation with and without vacuum is about 50 μm at the worst location, where the antechamber is wide and the thickness only 1 mm as predicted by the finite element simulations (FEA). Without the cold working method described above, plastic deformations of up to 700 μm were observed at the most critical location where the chamber is wide and after the first bakeout procedure at 200° C. More than 50 chambers were produced with this manufacturing procedure, and all chambers were UHV leak tight and fulfilling the dimensions specifications.

3. NEG coating

To coat the vacuum chamber inner surface with non-evaporable getter material (NEG) [30], a dedicated magnetron sputtering setup has been prepared at PSI with the help of experts from CERN [31]. The vacuum chamber that needs to be coated is mounted between two DN250 double crosses (Fig. 12). In the top double cross, are the high voltage feedthroughs to negatively bias the cathodes. The cathodes consist of wires of Ti, V, and Zr that are twisted together to form a single wire of roughly 3 mm diameter. A viewport on the top flange allows the observation of the glow discharge with a camera during the coating process, which is very useful for quick qualitative checks of plasma position and shape. The krypton gas supply is also connected to the top double cross while the pumping station (primary with turbo pumps) is connected to the bottom double cross to ensure a good flow of the krypton from top to bottom and removal of outgassed contaminants. About half a kilogram of loads are attached at the bottom of the wires to apply a continuous stretching of the wires during dilatation. The sputtering process can heat up the wire significantly, leading to the dilatation of the wire.

To generate the plasma, the two cathodes are biased negatively with power supplies delivering constant current. In addition, two short solenoids, stacked together with a total length of 210 mm and an inner diameter of 340 mm

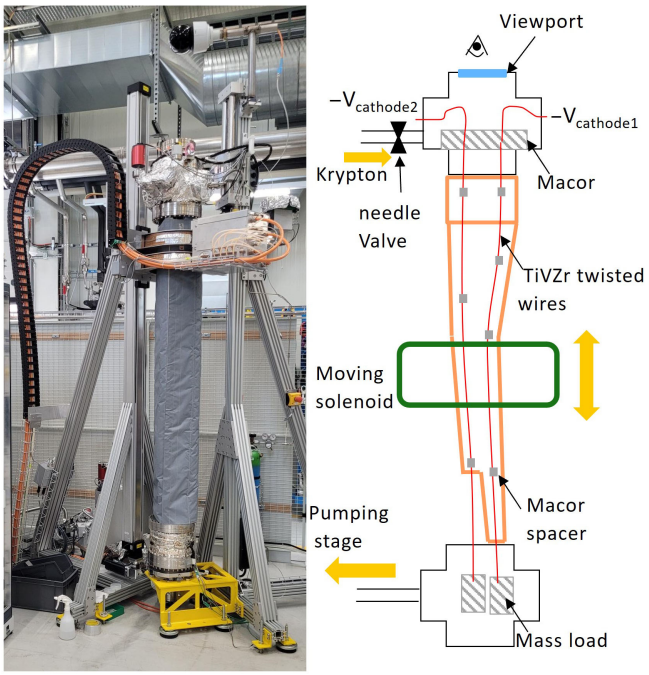

FIG. 12. NEG coating setup for SLS 2.0 vacuum chambers.

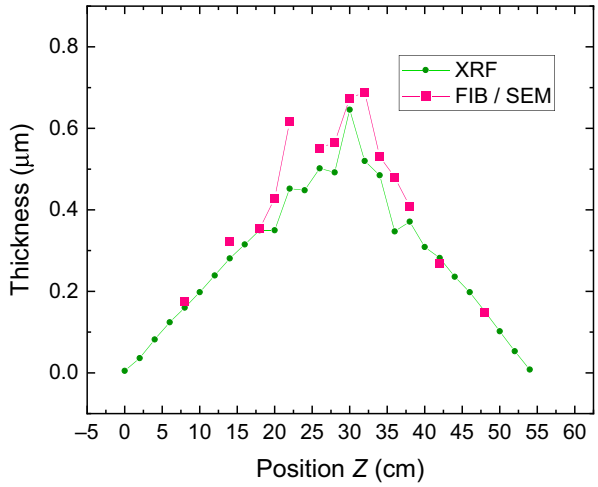

FIG. 13. NEG thickness distribution along an 18 mm dummy diameter copper pipe after 3H45 of coating at 0.03 mbar of Krypton, 400 G, 20 mA constant current, and about 300 V and with solenoids being kept at one fixed location. The thickness was measured with a focused ion beam-scanning electron microscope (FIB-SEM) and an x-ray diffraction technique.

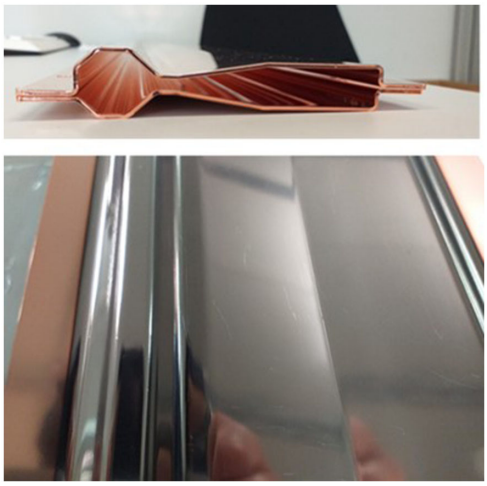

FIG. 14. Dummy copper plates to mimic SLS2 vacuum chamber geometry and find best parameters for NEG coating (as done by CERN for MAX IV [32]).

surround the chamber. This double solenoid is mounted on a motorized stage and can move vertically. Conditions of pressure, solenoid field, and plasma current are chosen such that the glow discharge is localized only where the solenoid is positioned. Deposition tests, with the solenoids being static at one location, showed that the NEG deposition follows a triangular distribution of 200 mm FWHM length along the chamber axis, and with typical conditions of deposition (Fig. 13). The solenoid, and thus, the plasma, is then moved up and down more than a 100 times along the chamber during the coating procedure of dipole chambers at a speed of around 4 mm/s. This technique of moving a short plasma relatively fast has the advantage of providing a good thickness uniformity over the length of the chamber, due to the many passes, and avoiding too much heat up of the cathode. The 200 mm long plasma is continuously displaced along the wire. Another advantage of a short plasma is that the glow discharge can spread itself according to the local geometry where the solenoids are located, and it is not dominated by a more favorable cathode-to-wall distance somewhere else in the chamber. The plasma voltage is also changing according to the geometrical changes during motion. Two wires are used to coat the CBN chamber with one wire in the electron channel and one wire going through the antechamber (Fig. 9). Macor spacers are used to avoid direct contact between cathodes and vacuum chamber.

After the coating procedure, the chamber is inspected with an endoscope to check that there is no delayering and that all surfaces are coated. A witness probe (coupon) is coated together with the chamber and is then analyzed by x-ray diffraction to measure the thickness and composition. The x-ray diffraction device has been calibrated against measurements done with a focused ion beam (FIB)/electron microscope (SEM) assembly. The measurements on the coupons showed that it requires 17 h of coating (with parameters of Table IV) to deposit about 0.5 μm thickness

TABLE IV. Golden parameters used for the NEG sputtering of CBN chambers.

Krypton pressure	0.035 mbar
Solenoid peak field	400 Gauss
Glow discharge current	20 mA
Typical glow discharge voltage	215–280 V
Typical distance cathode-chamber wall	7.5 mm with 18 mm chamber inner diameter
Chamber inner diameter	18 mm (12 mm height in antechamber)
Twisted wires of Ti, Zr, and V	3 times 1 mm diameter wires
Duration	17 h for 0.5 μm thickness
Solenoid moving speed	4.1 mm/s
Solenoid scanning length	1760 mm
Thickness goal	0.5 ± 0.2 μm
Composition	Ti: 10%–50%; Zr: 15%–50%; V: 15%–50%

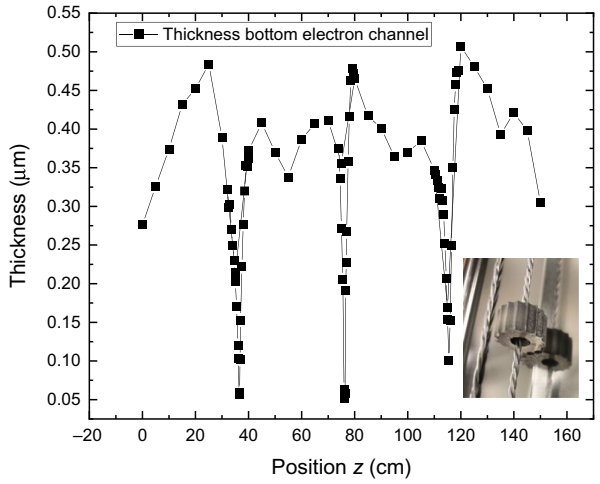

FIG. 15. Distribution profile of NEG thickness along the dummy test chamber axis using 0.03 mbar of Krypton, 400 G, 20 mA, and a solenoid motion speed of 0.4 mm/s during 12 h. The dips on the profile are due to the Macor spacer (example in the picture inset).

of TiZrV. The layer compositions given by XRD is also within the specifications. Several tests with dummy half shells [32] (Fig. 14) were performed to find out the ideal coating parameters, which maximize the coverage, and lead to the desired thickness. These parameters are summarized in Table IV and lead to a deposition rate of about 3 mm^3/h, in the electron channel. This deposition rate corresponds to the integral of the thickness profile of Fig. 13 multiplied by the circumference of the 18 mm diameter copper pipe. This rate is used to determine the duration required for the coating of a long CBN chamber with a moving plasma (17 h for 1760 mm chamber length). The tests with the half shells plates also showed that the uniformity of the thickness decreases significantly over a portion of about five centimeters around the Macor spacers (Fig. 15). The final positions of Macor spacers in the CBN chamber are indicated in the schematic of Fig. 12. Also the layer composition exhibits a regular pattern along the cathode axis, which corresponds to the twist periodicity of the three wires combination Ti, V, and Zr, which is, in our case, about 20 mm (Fig. 16). On average, the obtained alloy composition is well within the specifications and should guarantee an activation at a temperature around 180 °C.

The dipole chambers produced at PSI were all coated using the above described recipe. All the other chambers (e.g., CSS and CRM) were produced and coated by the industry [33]. Every chamber is inspected with an endoscope to check that there is no delayering of the NEG coating and to estimate the surface coverage. Uncoated areas are easy to detect optically on copper since NEG color is metallic gray, which contrasts with the orange of copper. We achieve, in general, about 99% of surface coverage and only small areas where the Macor spacer was sitting are left uncoated (red marked zone in Fig. 17).

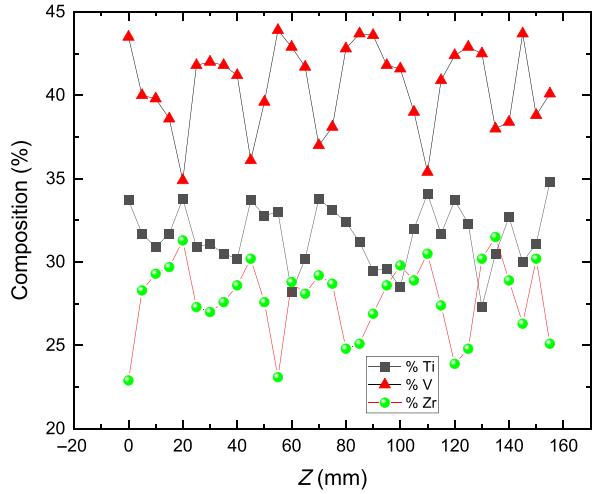

FIG. 16. Composition of the NEG layer along the half plate axis.

4. Dipole chamber activation

To finally assess the quality of the NEG coating, the first produced CBN chamber was activated to 200° C and then isolated from its pumping station to measure the achieved ultimate pressure (Fig. 18) [31]. When closing the valve, the pumping speed of the NEG layer should compensate for the outgassing of the uncoated areas of the stainless-steel pump block including the right-angle valve. Indeed, after closing the valve the pressure dropped in a few hours by roughly an order of magnitude to reach 10^{-10} mbar on the pump block side and 4×10^{-11} mbar at the other extremity of the chamber. Cold cathode gauges IKR270 have been used for this measurement. The influence of the gauge itself on the measured pressure is not negligible in the setup but there is a net pumping effect of the NEG coating. Pressure is larger at the cube extremity due to the uncoated surfaces, but it does not affect the other extremity of the chamber due to the small conductance. The drop in pressure by 1 order

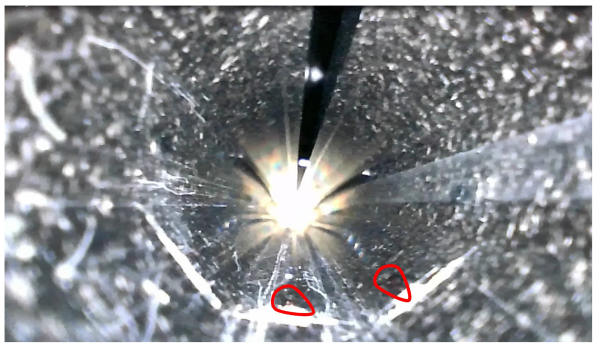

FIG. 17. Endoscope picture of the octagonal electron channel of a CBN chamber after NEG coating. Copper color can be detected in two small areas (marked red) where the Macor spacer was located.

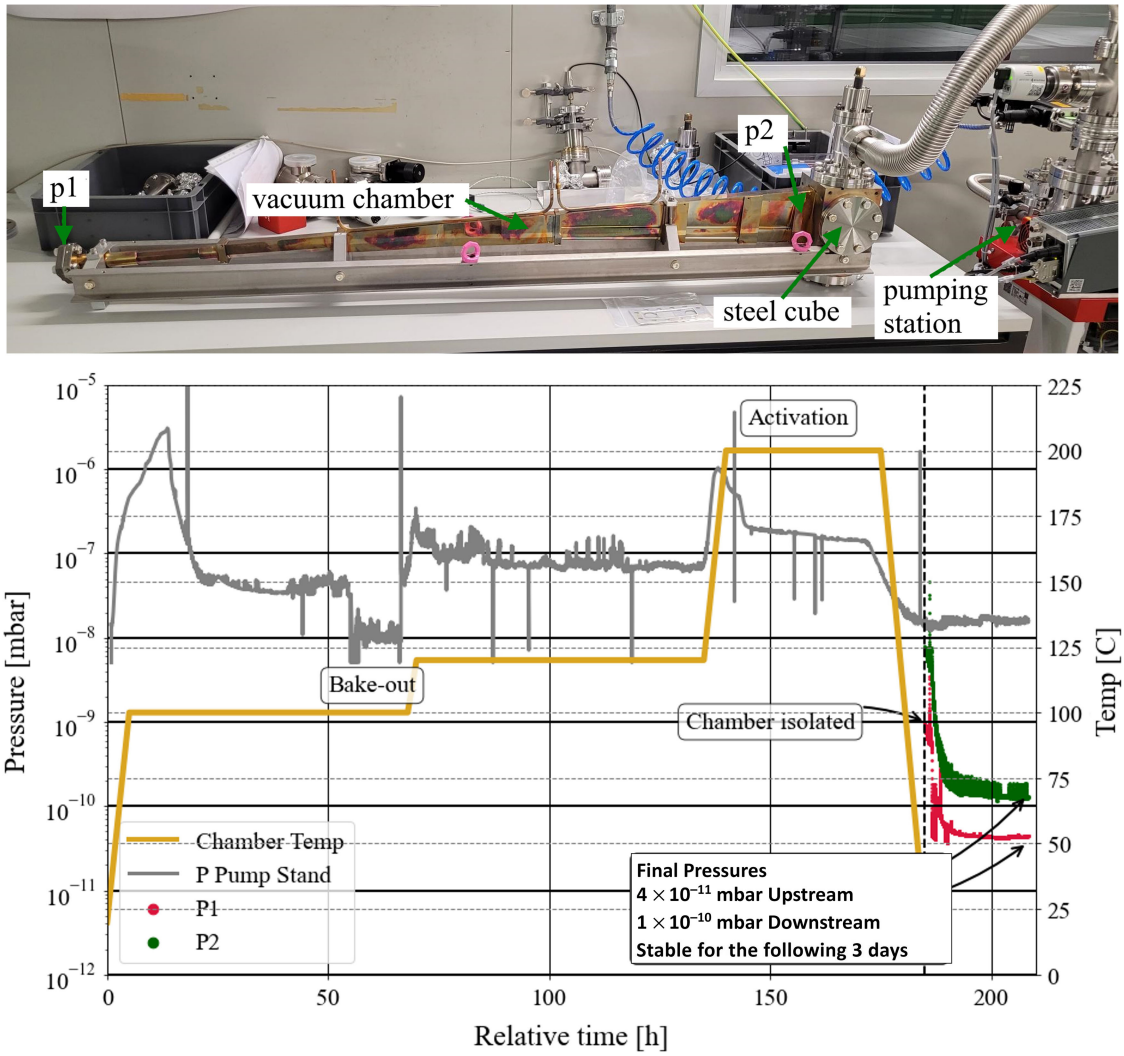

FIG. 18. CBN dipole chamber connected to a pump station for NEG activation test.

of magnitude demonstrates the pumping effect of the NEG layer.

C. Crotch absorbers

The main constraint of the absorber is to fit in the DN63 port of the CBN cube, which means that the narrow and intense SR beam is spread over about 60 mm length at maximum [34]. Most of the absorbers of SLS 2.0 are designed to absorb at least 3.7 kW coming from the standard bending magnets and for peak power density at normal incidence as high as 600 W/mm^2. There are, however, also 5 T superconducting bending magnets in the ring generating up to 7 kW of power with peak power density at normal incidence as high as 1100 W/mm^2 [14]. To absorb such high power, Glidcop AL-15 is used as a base material due to its high resistance to thermal stress [26] (up to 400 °C is possible), and the two jaws will have an inclination of only 1° so that the power density gets reduced to less than 30 W/mm^2 (this inclination is 3° for the normal bending magnet absorbers). In addition, the teeth top and bottom are interleaved such that power gets equally distributed between top and bottom cooling channels (Fig. 19). The maximum temperature of the 5 T superbend absorber will be about 300 °C on the surface near the window. A negative consequence of the small jaw angle is that the opening of the absorber is limited to ±0.75 mm. As a result, the vertical beam orbit variation, with full power, will be limited to ±250 μm to ensure that the SR fan arrives on the inclined surfaces. Temperature sensors will help to detect overheating for the very first commissioning days until the beam position monitors (BPM) are calibrated and can be used to limit the vertical beam offsets. Six stainless steel tubes are penetrating the Glidcop jaws and water is entering from the inner part of the stainless-steel channel and coming out through the small interspace between steel outer diameter and Glidcop hole. The water from all six channels comes together in a distribution block.

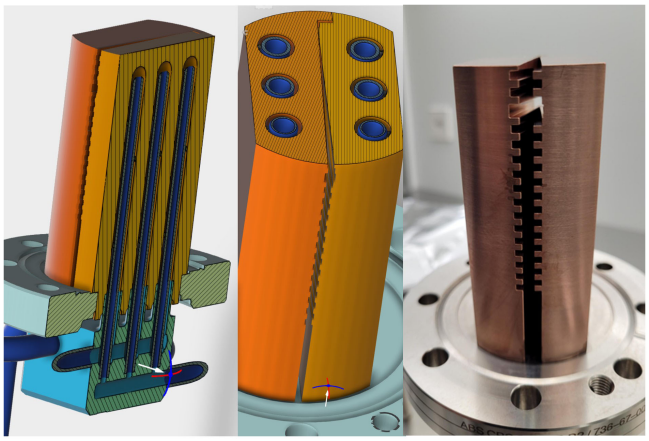

FIG. 19. Cut views of the Glidcop absorber that has an opening angle of 2° for the superconducting superbend magnet (3D views courtesy of FMB GmbH) and picture of a normal bend absorber (3° opening).

The Glidcop jaws are brazed together with the flange and the cooling channel distribution block in one step [33].

D. Beam position monitors (BPM) chambers

The beam position monitor (BPM) vacuum chamber combines the button BPM pickups [35] together with a small pipe where the horizontal and vertical steerers are located, the so-called CSS chamber (Fig. 20). There are nine such BPM CSS chambers per arc. The full chamber is in stainless steel coated with 5 μm of copper and 0.5 μm of NEG on top of it. The stainless-steel wall thickness is only 0.5 mm thick at the location of the steerers to ensure good transmission of the fast-changing magnetic field of the corrector magnets. The copper layer of 5 μm, on the other hand, ensures a good electrical conductivity for beam Eddy current without deteriorating much the magnetic field transmission. The inner section is an octagonal shape with 21 mm distance between opposite sides. The octagonal shape suits well the installation of the pickups which are TIG welded in a 316LN, 3D forged, body. With 21 mm, the rf pickups stay in the shadow of the upstream 18 mm section preventing any direct SR heat up of the stainless-steel parts and especially of the button rf pickups. SYNRAD simulations have shown that reflected photons can end up on the pickup. The simulated hit rate is less than 10^{14} photons s^{-1} cm^{-2} with photons of less than 100 eV, which might be enough to generate small photoemission current from the pickups.

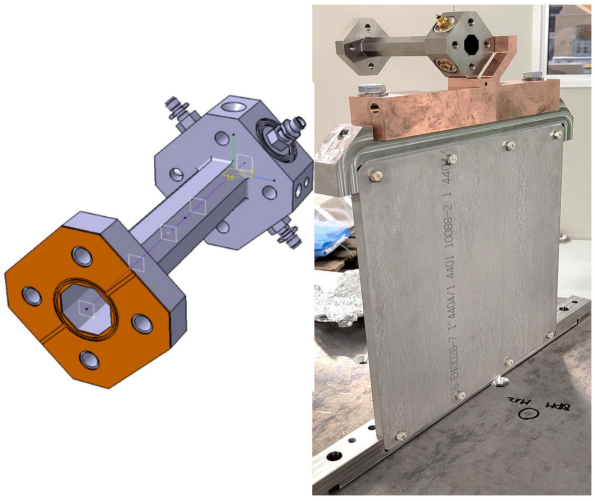

FIG. 20. Chamber straight steerers (CSS) includes the BPM pickups (left part) and chamber support (right).

The BPM block is supported on the girder thanks to a double plate support. This design prevents the transverse motion of the BPM while permitting longitudinal motion. Damping material (balsa wood) is glued with viscoelastic adhesive between the two plates to attenuate the high frequency vibrations amplitude. A survey reference cone (fiducial) on the BPM body allows a precise positioning by shimming method.

The position stability of the BPM is essential to permit fast orbit feedback and obtain the best possible SR pointing stability for the users. Considering the SR power heat up of Fig. 5, finite element mechanical analysis has shown that the CSS chamber will be the warmest point of the arc at about 60 °C (Fig. 21). The CSS chamber is attached to a CuCrZr support, which is water cooled to make a thermal barrier between the warm BPM and the cold girder restricting the dilatation drifts to the small CuCrZr part. Like that, the remaining drift of the BPM axis is about 5 μm vertically and 10 μm radially with or without beam (Fig. 21).

The string of chambers composing an SLS 2.0 arc is supported at each pump block (heaviest parts) and at each beam position monitor, which means that there is at least one support every 1.5 m. While the BPMs and CBN blocks are maintained at a stable position, the rest of the arc with its thin walls in copper gets deformed by the gravity, the outside atmospheric pressure, and the thermal dilatation. Overall, the largest deformation is located at the CBN level which has a maximum sagitta of 330 μm and a horizontal

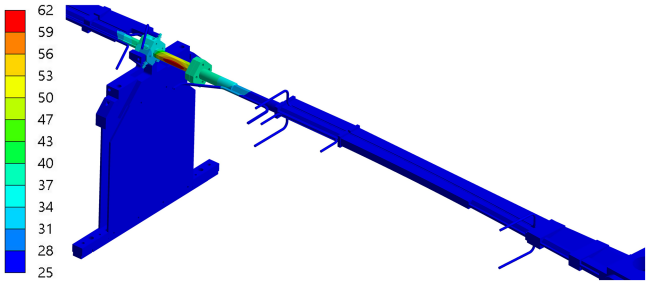

FIG. 21. FEA simulation of the temperature distribution (color scale in °C) around the BPM vacuum chamber (CSS) considering the SR heat dissipation and wakefield heating.

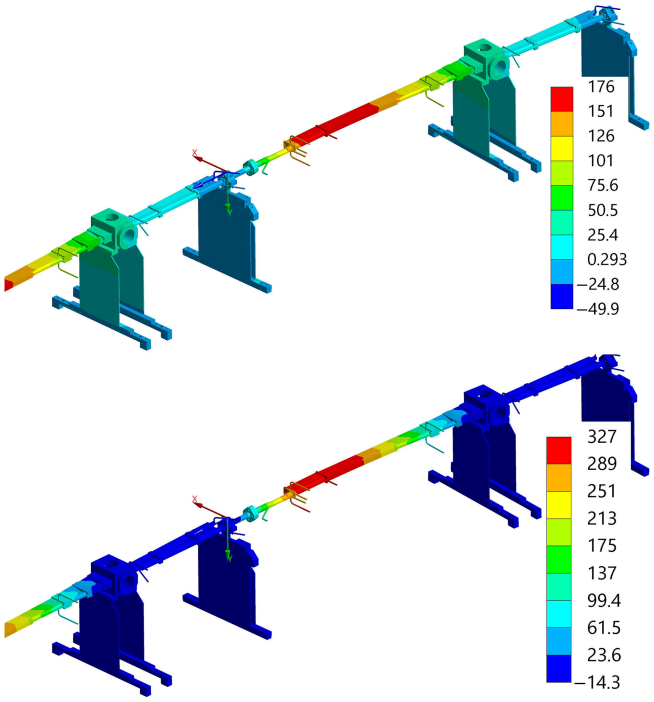

FIG. 22. FEA simulations of the mechanical deformation of an arc portion under SR power heat up as described in Fig. 5, gravity, and atmospheric pressure. The color scale corresponds to micrometers of deformation in the horizontal plane (top) and vertical plane (bottom).

deformation due to dilatation of 180 μm toward the outer ring (Fig. 22). These deformations are, however, in the elastic regime despite a low yield strength after the brazing process. The pressure and gravity effect could be verified during arc assembly (see next section).

A negative consequence of this mechanical deformation is that the chambers is in direct contact with most of the magnet poles (no spacers or foils are for the moment foreseen between poles and copper chambers). On the other hand, the flexibility of the thin walls vacuum chambers also gives the possibility to adjust the vacuum chamber position to fit the magnet apertures along the arc.

IV. ARC ASSEMBLY AND ACTIVATION

A. Arc assembly and transport

Each arc is assembled in a clean room (class 10 000) and consists of 28 chambers of different types (Fig. 23) screwed together with flat gaskets (Fig. 24). These flat gaskets are in copper with a 5 μm thick silver coating and a sealing lip of 200 μm thickness on both side. We measured that when the flanges are tightened together with 30 Nm moment, the lip is compressed by 100 to 200 μm leaving short gaps discontinuities of less than 100 μm at each flange/gasket transition.

These gaps are seen by the beam and have thus been integrated with the broadband impedance budget of the

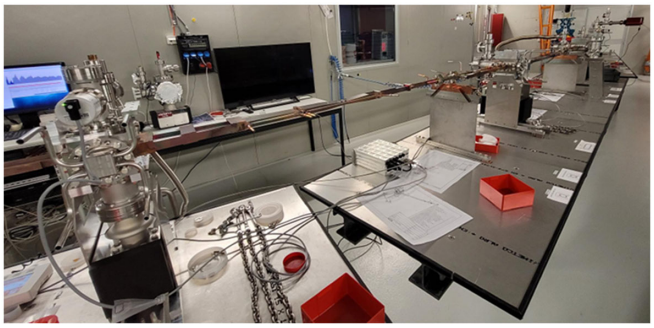

FIG. 23. Picture of the arc chambers under assembly.

storage ring vessel [28]. The octagon inner diameter of the flat gaskets is also 0.4 mm larger than the flange aperture in order to avoid the gasket material protruding into the vacuum chamber when compressed (i.e., 21.4 mm for flanges that have 21 mm diameter). Compared to other sealing systems, it requires less longitudinal space to dismount a chamber out of the arc when no bellow is present. There are 30 flat gaskets per arc.

At the end of the assembly, precise positioning of the seven crotch absorbers is performed with a laser tracker (especially the pitch angle of the absorber flange cannot be corrected anymore once it is tightened). This should ensure that the SR fan is well distributed between the upper and lower jaws of the absorbers. The vertical and horizontal positions of pump blocks and BPMs are adjusted within 100 μm to ensure the best fit of the chambers in the

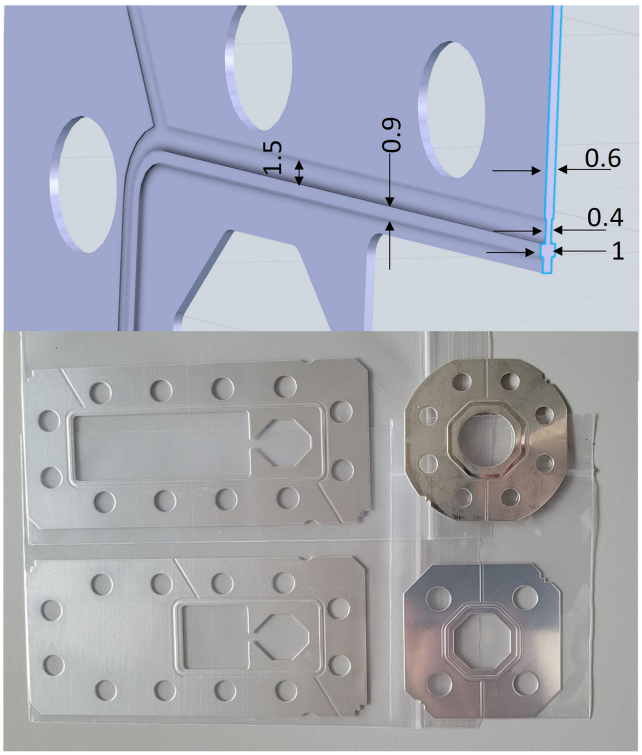

FIG. 24. Flat gasket design to seal chambers together.

FIG. 25. Picture of the vacuum arc attached to a transport frame with chains and stiffened with alu T-shaped profiles (top) and arc being transported with the hall crane (bottom).

magnet's apertures. The arc is then evacuated with two turbo pumps to less than 10^{-6} mbar and tested for leaks larger than 2×10^{-10} mbar l s^{-1}.

The vacuum chamber arc is then attached to a stiff transport frame. All heavy parts, the pump blocks, and the gate valves are attached with stainless-steel chains to this transport frame. All the transport tooling parts are made of nonmagnetic materials to avoid the interaction with the permanent magnets during the assembly in the tunnel. In addition, aluminum T-shaped profiles connect pump blocks together to give more rigidity and avoid the risk of chamber deformation during transport. The copper chamber and BPMs are attached to this aluminum stiffener (Fig. 25). Finally, the transport frame is attached to a crane lifting beam and transported into an 18-m-long oven for the bakeout and activation procedure.

B. Arc activation

When the arc is installed in the oven (Fig. 26), seven turbo pumps station (HiCube 80 Eco from Pfeiffer) with 35 l/s equivalent N2 pumping speed, are connected to the CF40 right-angle valves of each pump block of the arc. There are three pressure gauges (cold cathode gauges IKR 270 from Pfeiffer) mounted on the first, last, and middle CBN, respectively. Five arcs are also equipped with rest gas analyzer (RGA) QMG 220 PrismaPlus from Pfeiffer.

Prior to activation of the NEG coating layer, the whole arc is heated up to 130 °C for more than 48 h (Fig. 27) to desorb most of the water, especially from the noncoated

FIG. 26. Vacuum arc with its frame installed in the oven (left) is pumped with turbo-pump/primary pump stations during the heat up cycle (right).

areas like the pump blocks, the ion getter pumps, and the Glidcop crotch absorbers. The seven ion getter pumps are regularly switched on for a few minutes to accelerate the outgassing of pump surfaces during this first phase. After this first cycle at 130 °C, the temperature is raised to 200 °C for a period of 24 h at minimum to activate the thin NEG layer deposited on the vacuum vessel's inner surface. During the rise of the temperature to 200 °C, the getter pumps are activated with about 100 W (less than 5 A current) of electrical power for about 1 h. This activation and also the ion pump flashing cycles generate peaks of pressure visible on the pressure evolution curve (Fig. 27). At the end of the 200 °C activation period, the ion pumps are switched on definitively. Once the chamber has cooled down to around 80 °C, the three cold cathode pressure gauges of the arc are connected and switched on. Once the gauges have desorbed most of their contaminants and the arc is at room temperature, the valves isolating the turbo stations are closed. Closing the valves is followed by a

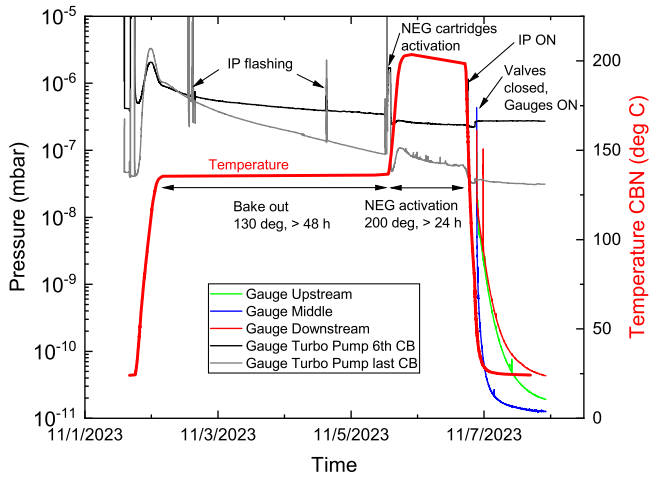

FIG. 27. Pressure evolution in the vacuum arc during the baking and activation procedure (1 week).

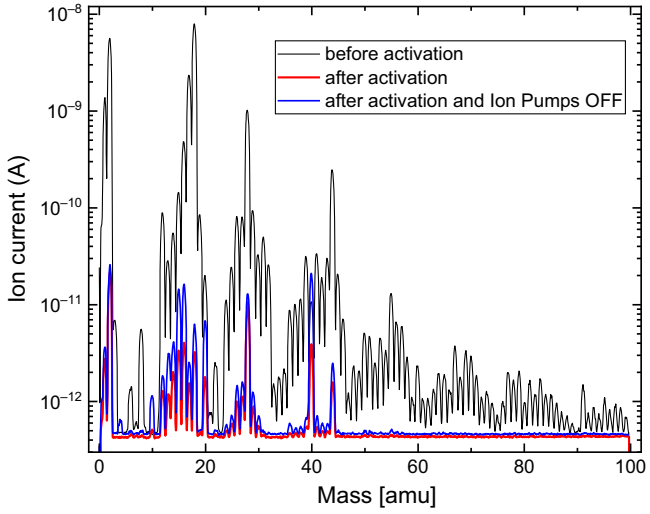

FIG. 28. Rest gas mass spectrum measured in the pump block situated in the center of the arc.

FIG. 29. Arc vacuum chamber installation in the magnets when the top half part is removed (left and middle). The BPM chambers are guided with a stainless-steel rod during the final lowering of the arc (middle). Contact with poles occurs at several locations like the sextupoles (right).

rapid drop of the pressure by about 2 to 3 order of magnitude from $10^{-8} - 10^{-9}$ to $10^{-10} - 10^{-11}$ mbar in less than 10 h thanks to the pumping of the NEG layer.

It is possible that the pressure inside the NEG-coated copper chamber is smaller than in the pump blocks as it was observed with the activation of a single CBN chamber (see above). Indeed, gauges are installed in the pump blocks that have large uncoated areas like the Glidcop absorbers or the right-angle valves. Nevertheless, with pressure around 10^{-11} mbar (actually below the specified measuring range of the IKR270 gauges), the requirements for the SLS 2.0 storage ring is fulfilled.

The RGA spectrum (Fig. 28) does not show the presence of any suspicious contaminants before activation and is dominated by water. After bakeout and NEG activation, the water peaks decrease significantly, and pressure is dominated by hydrogen and carbon monoxide (CO). All peaks above 40 amu (with the exception of amu 44 CO_2) represent much less than 1% of the total pressure. The series of peaks around amu 15 correspond to the CH molecules (methane in particular). If the ion pumps of the cubes are switched off one can notice that mainly the peak of Argon (amu 40) and the methane (CH_4, amu 16) are rising since they are not pumped by the getter material of both the NEG layer and the getter cartridges Z400.

The final assembly of the arc vessel in the magnets was done for the first time in the arc ARS11 (Fig. 29). All the magnet's top half has been dismounted, and the C-shaped permanent magnet dipoles were simply shifted on the side of the girder. During the lowering of the vacuum arc chamber into the magnets, guiding rods attached to the girder were inserted in specific holes of the CuCrZr BPM support (white arrows in Fig. 29 middle) to guide the whole arc into the magnets. Finally, the 17 m long arc chamber could eventually be installed in the magnet's apertures. After the alignment of the pump blocks and BPMs, the magnets top half could be closed. The copper chamber could fit well the magnet apertures but with contact to poles at several locations like the antibend magnets or the sextupoles. Contact between the vacuum vessel and poles should not be a problem as long as there is no shearing effect during the dilatation of the chamber at each beam on/off cycle.

V. CONCLUSION

Diffraction limited storage rings present several challenging requirements for vacuum vessels. The main differences with the previous generation of storage rings like SLS are the reduction of the cross section, the change of main material from stainless steel to copper, and the NEG coating of the inner surfaces. The overall design of the vessels of the SLS 2.0 storage ring has been described in detail from conceptual studies to production recipes and vacuum performances. Most important design choices are explained as well as weaknesses of the design. The assembled vacuum chamber arcs are fulfilling the requirements for SLS 2.0 storage ring operation.

[1] P. F. Tavares *et al.*, Commissioning and first-year operational results of the MAX IV 3 GeV ring, J. Synchrotron Radiat. **25**, 1291 (2018).

[2] S. White *et al.*, Commissioning and restart of ESRF-EBS, in *Proceedings of the 12th International Particle Accelleration Conference, IPAC-2021, Campinas, SP, Brazil* (JACoW, Geneva, Switzerland, 2021).

[3] L. Liu, M. B. Alves, F. H. D. Sá, R. H. A. Farias, S. R. Marques, A. C. S. Oliveira, X. R. Resende, R. M. Seraphim, and H. Westfahl, Status of sirius operation, in *Proceedings of the 13th International Particle*

Accelleration Conference, IPAC-2022, Bangkok, Thailand (JACoW, Geneva, Switzerland, 2022).

[4] A. Nadji, Synchrotron SOLEIL upgrade project, in *Proceedings of the 12th International Particle Accelleration Conference, IPAC-2021, Campinas, SP, Brazil* (JACoW, Geneva, Switzerland, 2021).

[5] C. Abraham *et al.*, Diamond-II conceptual design report, 2019, https://www.diamond.ac.uk/dam/jcr:ec67b7e1-fb91-4a65-b1ce-f646490b564d/Diamond-IIConceptualDesign-Report.pdf.

[6] F. Pérez *et al.*, Alba II accelerator upgrade project, in *Proceedings of the 13th International Particle Accelleration Conference, IPAC-2022, Bangkok, Thailand* (JACoW, Geneva, Switzerland, 2022).

[7] Conceptual design report synchrotron SOLEIL upgrade, https://www.synchrotron-soleil.fr/en/news/conceptual-design-report-soleil-upgrade/.

[8] E. Karantzoulis, A. Fabris, and S. Krecic, The Elettra 2.0 project, in *Proceedings of the 13th International Particle Accelleration Conference, IPAC-2022, Bangkok, Thailand* (JACoW, Geneva, Switzerland, 2022).

[9] Advanced photon source upgrade project final design report, Report No. APSU-2.01-RPT-003, 2019, https://www.aps.anl.gov/APS-Upgrade/Documents/.

[10] C. Steier, A. Anders, J. Byrd, K. Chow, and S. D. Santis, ALS-U: A soft x-ray diffraction limited light source, in *Proceedings of the 2nd North American Particle Accelerator Conference (NAPAC-2016) Chicago, Illinois* (JACoW, Geneva, Switzerland, 2016).

[11] R. Bartolini *et al.*, Status of the PETRA IV machine project, in *Proceedings of the 13th International Particle Accelleration Conference, IPAC-2022, Bangkok, Thailand* (JACoW, Geneva, Switzerland, 2022).

[12] Y. Asano *et al.*, SPring-8-II conceptual design report 2014, http://rsc.riken.jp/eng/pdf/SPring-8-II.pdf.

[13] Y. Jiao, X. Cui, Z. Duan, Y. Guo, and D. Ji, Accelerator physics studies for the high energy photon source (HEPS), in *Proceedings of the 60th ICFA Advanced Beam Dynamics Workshop on Future Light Sources (FLS2018) Shanghai, China* (JACoW, Geneva, Switzerland, 2018).

[14] H.-H. Braun, T. Garvey, M. Jörg, A. Ashton, P. Willmott, R. Kobler, and E. Zehnder, SLS 2.0 storage ring. Technical design report, 2021.

[15] A. Streun, M. Aiba, M. Böge, C. Calzolaio, M. Ehrlichman, M. Negrazus, B. Riemann, and V. Vrankovic, Swiss Light Source upgrade lattice design, Phys. Rev. Accel. Beams **26**, 091601 (2023).

[16] S. C. Leemann and A. Streun, Perspectives for future light source lattices incorporating yet uncommon magnets, Phys. Rev. ST Accel. Beams **14**, 030701 (2011).

[17] B. Riemann and A. Streun, Low emittance lattice design from first principles: Reverse bending and longitudinal gradient bends, Phys. Rev. Accel. Beams **22**, 021601 (2019).

[18] V. Ziemann and A. Streun, Equilibrium parameters in coupled storage ring lattices and practical applications, Phys. Rev. Accel. Beams **25**, 050703 (2022).

[19] C. Calzolaio, A. Gabard, P. Lerch, G. Montenero, M. Negrazus, S. Sanfilippo, S. Sidorov, and V. Vrankovic, Longitudinal gradient bend magnets for the upgrade of the Swiss Light Source storage ring, IEEE Trans. Appl. Supercond. **30**, 1 (2020).

[20] S. Sanfilippo, M. Aiba, C. Calzolaio, M. Duda, G. Montenero, R. Riccioli, S. Sidorov, and C. Zoller, Magnets for the upgrade of the Swiss Light Source at the Paul Scherrer Institute: Design, production, measurement challenges, IEEE Trans. Appl. Supercond. **34**, 4000105 (2023).

[21] P. Chiggiato and R. Kersevan, Synchrotron radiation-induced desorption from a NEG-coated vacuum chamber, Vacuum **60**, 67 (2001).

[22] E. Al-Dmour, J. Ahlback, D. Einfeld, P. F. Tavares, and M. Grabski, Diffraction-limited storage-ring vacuum technology, J. Synchrotron Radiat. **21**, 878 (2014).

[23] A. Gamelin and W. Foosang, Influence of the coating resistivity on beam dynamics, Phys. Rev. Accel. Beams **26**, 054401 (2023).

[24] M. Dehler *et al.*, rf characterization of thin NEG coatings in the sub-THz range, in *Proceedings of the International Workshop on Multipactor, Corona and Passive Intermodulation (MULCOPIM-2022), Valencia, Spain* (JACoW, Geneva, Switzerland, 2022).

[25] M. Dehler, Ion trapping and instabilities in SLS 2.0, in *Proceedings of the 14th International Particle Accelleration Conference, IPAC-2023, Venice, Italy* (JACoW, Geneva, Switzerland, 2023).

[26] X. Wang, C. Rosenberg, R. Ganter, A. Weber, M. Maehr, and S. Bugmann, Thermal calculation and testing of SLS 2.0 crotch absorbers, in *Proceedings of the 12th International Conference on Mechanical Engineering Design of Synchrotron Radiation Equipment and Instrumentation (MEDSI 2023), Beijing, China* (JACoW, Geneva, Switzerland, 2023).

[27] R. Kersevan and M. Ady, Recent developments of Monte-Carlo codes MOLFLOW+ and SYNRAD+, in *Proceedings of the 10th International Particle Accelleration Conference, IPAC2019, Melbourne, Australia* (JACoW, Geneva, Switzerland, 2019).

[28] A. Citterio, J. P. Braschoss, M. Dehler, S. Dordevic, D. Stephan, and L. Stingelin, Machine impedance calculation and optimization of vacuum components in SLS 2.0 in *Proceedings of the 14th International Particle Accelleration Conference, IPAC-2023, Venice, Italy* (JACoW, Geneva, Switzerland, 2023).

[29] R. Ganter *et al.*, SLS 2.0 vacuum components design, in *Proceedings of the 14th International Particle Accelleration Conference, IPAC-2023, Venice, Italy* (JACoW, Geneva, Switzerland, 2023).

[30] P. Chiggiato and P. Costa Pinto, Ti–Zr–V non-evaporable getter films: From development to large scale production for the Large Hadron Collider, Thin Solid Films **515**, 382 (2006).

[31] N. Kirchgeorg, J. Buchmann, N. Gaiffi, R. Ganter, P. Huber, M. Magjar, C. Rosenberg, and D. Stephan, A new NEG coating setup with travelling thin solenoids for the SLS 2.0 complex vacuum chambers, J. Phys. Conf. Ser. **2687**, 082028 (2024).

[32] S. Calatroni, P. Chiggiato, P. C. Pinto, M. Taborelli, M. Grabski, J. Ahlbäck, E. Al-Dmour, and P. F. Tavare, NEG thin film coating development for the MAX IV vacuum system, in *Proceedings of the 4th International Particle Accelerator Conference, IPAC2013, Shanghai, China* (JACoW, Geneva, Switzerland, 2013).

[33] FMB GmbH, https://www.fmb-berlin.de/index.php/de/ (2023).

[34] C. Rosenberg *et al.*, SLS 2.0 crotch absorbers design, in *Proceedings of the 14th International Particle Accelleration Conference, IPAC-2023, Venice, Italy* (JACoW, Geneva, Switzerland, 2023).

[35] B. Keil, R. Ditter, F. Marcellini, G. Marinkovic, J. Purtschert, M. Rizzi, M. Roggli, D. Stephan, and X. Wang, Development of the SLS 2.0 BPM system, in *Proceedings of the 12th International Beam Instrumentation Conference (IBIC 2023), Saskatoon, Canada* (JACoW, Geneva, Switzerland, 2023).